ACS APPLIED MATERIALS & INTERFACES

Research Article

www.acsami.org

Ultrathin, Single-Crystal WO_3 Nanosheets by Two-Dimensional Oriented Attachment toward Enhanced Photocatalystic Reduction of CO_2 into Hydrocarbon Fuels under Visible Light

Xiaoyu Chen,[†,§] Yong Zhou,[†,‡,*] Qi Liu,[†,§,∥] Zhengdao Li,[†,§] Jianguo Liu,[†,§] and Zhigang Zou[†,‡,§,*]

[†]Eco-Materials and Renewable Energy Research Center (ERERC), National Laboratory of Solid State Microstructures, [‡]School of Physics, and [§]Department of Materials Science and Engineering, Nanjing University, Nanjing 210093, P. R. China

[∥]Anhui Polytechnic University, Wuhu 241000, P. R. China

Supporting Information

ABSTRACT: An ultrathin, single-crystal WO_3 nanosheet of ~4−5 nm in thickness, corresponding to six repeating unit cells of monoclinic WO_3 along the *c* axis, was synthesized with laterally oriented attachment of tiny WO_3 nanocrystals formed using a solid−liquid phase arc discharge route in an aqueous solution. Size-quantization effects in this ultrathin nanostructure alter the WO_3 band gap to enable the nanosheet to exhibit enhanced performance for photocatalytic reduction of CO_2 in the presence of water in hydrocarbon fuels that do not exist in its bulk form.

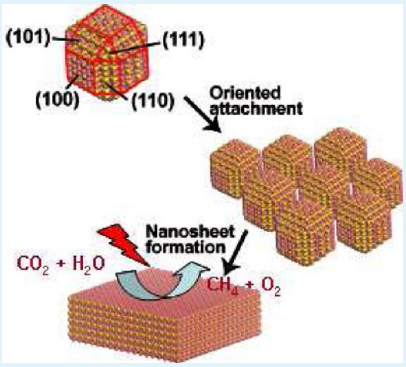

KEYWORDS: *WO_3, nanosheets, ultrathin, photocatalysis, CO_2 reduction, renewable fuel*

INTRODUCTION

Two-dimensional (2D) anisotropic nanostructures of metal oxides and semiconductors, especially ultrathin nanosheets (thickness < 5 nm), possess pronounced quantum surface effects and dramatic changes in electronic structures and thus in the physical and chemical properties, which are anticipated to inspire new fundamental and technological research.[1] Such nanosheets are expected to bridge the gap between the quantum world of zero- or one-dimensional nanomaterials and three-dimensional macroscale bulk materials.

Controlled assembly of nanoparticle building blocks into large, anisotropic objects is one of the most promising approaches in the field of materials research, but it presents a conceptual challenge. Organic ligand molecules generally play a crucial role in such processes by capping nanoparticle surfaces selectively and may hinder, modify, or trigger an oriented attachment. Nanocrystals made of semiconductors, such as CdSe,[2] PbS,[3] and CeO_2,[4] can self-organize into free-standing nanosheets in a solution phase. The involved formation mechanisms include oriented attachment and self-organization of initially formed small nanocrystals followed by an in situ recrystallization process.

Tungsten oxide is known as a multifunctional material with electrochromic,[5] optochromic,[6] and gasochromic properties[7,8] and photocatalytic applications.[9] WO_3 flakes can be obtained by various techniques including high-temperature anodization,[10] as well as by hydrothermal,[11] solvothermal,[12,13] acid etching,[14] and mechanical exfoliation.[15,16] However, flakes made by these techniques suffer from inhomogenous thickness and are also generally too thick (>20 nm) for efficient photogenerated electrons and holes transport to the surface.[17,18]

In this paper we for the first time report an ultrathin, single-crystal WO_3 nanosheet of ~4−5 nm in thickness, close to the Bohr radius for the material (~3 nm)[19] and corresponding to six repeating unit cells of monoclinic WO_3 along the *c* axis. The WO_3 growth starts with 4−5 nm-size seeds formed using a solid−liquid phase arc discharge (SLPAD) route in an aqueous solution, which has been used for preparing silver nanowires[20a] and CuO nanorods.[20b] With aging time, the tiny WO_3 seeds subsequently extend laterally to form the nanosheet. The nanosheet thickness is fixed by the seed dimension, keeping constant during the growth, confirmed with small-angle X-ray diffraction (SAXRD) patterns. Relative to reported ligand-driving 2D crystal growths,[2−4] the present 2D construction of single-crystalline WO_3 involves no use of any surfactants. Size-quantization effects in this ultrathin nanostructure alter the WO_3 band gap to enable the nanosheet to exhibit enhanced performance for photocatalystic reduction of CO_2 in the presence of water in hydrocarbon fuels that do not exist in its bulk form.

Received: February 6, 2012
Accepted: June 27, 2012
Published: June 27, 2012

EXPERIMENTAL SECTION

Preparation of the Tiny WO_3 Seeds and Subsequent Growth of the Nanosheets. The setup of the SLPAD for the growth of WO_3 seeds and subsequent growth of the nanosheets is schematically illustrated in Figure S1 (Supporting Information). Two high-purity tungsten filaments (ca. 5 mm in diameter) were served for two electrodes. First, one of the electrodes was put into a beaker containing a 0.1 mol/L $NaNO_3$ solution. Using an alternating current step-down circuit, a certain voltage (~150 V) was used between the two electrodes. Then, we brought the other electrode into contact with the surface of $NaNO_3$ solution momentarily. The arc discharge spark could be observed on the surface of the tungsten electrode and a continuous dissolution of the tungsten electrode because of the great exothermic during the solid−liquid phase arc discharge. Tiny tungsten trioxide nanoparticles were thus immediately produced in solution. With aging time for 12 h, the yellow precipitate was observed at the bottom of solution, which was separated by high-speed centrifugation and washed with distilled water and absolute ethanol several times and then was dried in a vacuum at 60 °C for 2 h.

Characterization. The crystal structures of the powder samples were investigated by an X-ray diffractometer (XRD) (Rigaku Ultima III, Japan) using Cu Kα radiation (λ= 0.154178 nm) at 40 kV and 40 mA. The XRD patterns were obtained over the scanning range of 10−80° at room temperature with a scan rate of 10° min^{-1}. The morphology of the powders was examined by field emission scanning electron microscopy (FESEM, FEI NOVA NANOSEM 230). Transmission electron microscopy (TEM) images and high-resolution transmission electron microscopy (HRTEM) images were obtained on a JEOL JEM-2100 microscope with a LaB6 filament and an accelerating voltage of 200 kV.

Measurement of Photocatalytic Activity. The photocatalytic reduction of CO_2 was carried out with 0.1 g of the powdered photocatalyst, which was uniformly placed at the bottom of a Pyrex glass cell. The reaction was in a gastight system. A total of 0.4 mL of didistilled water was injected into the system, which was filled with CO_2 to generate water vapor. After adsorption of CO_2 had reached equilibrium in the dark, light photoirradiation was performed using a 300 W Xe arc lamp equipped with a UV cutoff filter (λ > 420 nm). A gas pump was used to accelerate gas diffusion. The concentration of product in the tube was withdrawn with a gastight syringe and detected by gas chromatograph (Shimadzu, GC-14B with FID detector, Japan). The quantification of CH_4 yield was based on the external standard and the use of calibration curve. As a comparison, the commercial WO_3 powder was purchased from Sinopharm Chemical Reagent Co. Ltd.

RESULTS AND DISCUSSION

Transmission electron microscopy (TEM) images clearly reveal light contrast of the 2D nanostructures of the WO_3 (Figure 1 and Figure S2, Supporting Information). The nanosheets possess regular edges, and the lateral dimensions reach hundreds of nanometers. A HRTEM image shows the clear lattice fringes, perfectly aligning across the surface (Figure 1b), indicating a single-crystalline structure of the WO_3 nanoplate. The distances of the 2D crystal lattices are 3.77 Å and 3.65 Å, respectively, which can be indexed to (020) and (200) planes of monoclinic WO_3. The corresponding fast Fourier transform (FFT) pattern shows an ordered array of spots (the inset of Figure 1b), which can confirm the single crystallinity. An HRTEM image of a vertically standing nanosheet shows the basal (002) plane with the lattice fringe of $d_{(002)}$ = 3.84 Å (Figure 1c). These data demonstrate that the laminar shape of monoclinic WO_3 structure grows preferentially along the {100} and {010} surrounding planes and was enclosed by {001} top and bottom surfaces. A crystalline model of the nanosheet can thus be schematically illuminated in Figure 1d. The atom force microscopy (AFM) observation of the single nanosheet also

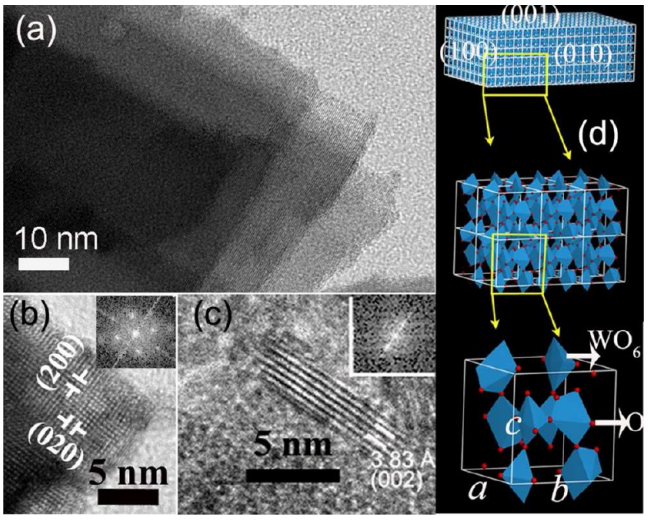

Figure 1. (a) TEM image of the WO_3 nanosheet, the HRTEM images of (b) the flat-laying and (c) the vertically standing nanosheet, the insets for corresponding FFT patterns, (d) crystalline model of the nanosheet.

corroborates the nanosheet thickness of ~4.5 nm (Figure 2). A total height of approximately 9.0 nm was also found, which corresponds to the height of two stacking nanosheets.

All XRD peaks of the formed nanosheet can be indexed to the monoclinic WO_3 crystal structure with a = 0.7301 nm, b = 0.7539 nm, and c = 0.7688 nm (JCPDS Card No. 83-0950) (Figure 3). No peaks associated with other compounds were detected, indicating that the WO_3 product is a pure phase. The stronger intensity of the (002) diffraction peak of the nanosheet relative to commercial polycrystalline powder and standard JCPDS card indicates a preferential orientation of the sheets in the (002) direction, consistent with the above high-resolution transmission electron microscopy (HRTEM) observation. The SAXD pattern shows that the nanosheet displays strong basal peaks up to the third high order line (Figure 4a), which is in accord with the thickness of the lamellar WO_3 nanosheets and assignable to the (00l) reflections of the lamellar sheet nanostructures, proving highly uniform thickness. The thickness is calculated to be 4.5 nm, well corresponding to six repeating unit cells, that is, 6 × 0.7688 nm = 4.6128 nm.

The Raman scattering spectrum also confirms the formation of the WO_3 nanoplate, showing the two strongest peaks at 720 cm^{-1} and 813.5 cm^{-1} assigned to the stretching vibration of tungsten atom with neighboring oxygen atoms [υ(O−W−O)] (Figure 5). The peaks at around 280.5 cm^{-1} accounts for the bending vibration [δ(O−W−O)]. The peak at around 954 cm^{-1} is attributed to the terminal —W═O bonds.[21]

Electron microscopy was used to elucidate the formation mechanism of the present WO_3 nanosheets. Great exotherm during the solid−liquid phase arc discharge allows the tungsten metal electrode to continuously dissolve in the form of clusters into aqueous solution. The highly active metal clusters were quickly oxided into tungsten oxide in the presence of water, as our previously reported preparation of CuO nanorods with the same SLPAD route.[20b] Tiny tungsten oxide nanocrystals with uniform sizes of ~5 nm were observed in great abundance at the early stage (t = 30 min) (Figure 6), which was also confirmed with the SAXRD pattern of the nanocrystals, exhibiting a distinct diffraction peak at 2θ = 2.0° (Figure 4b). With prolonging the aging time, the nanocrystals fused in two

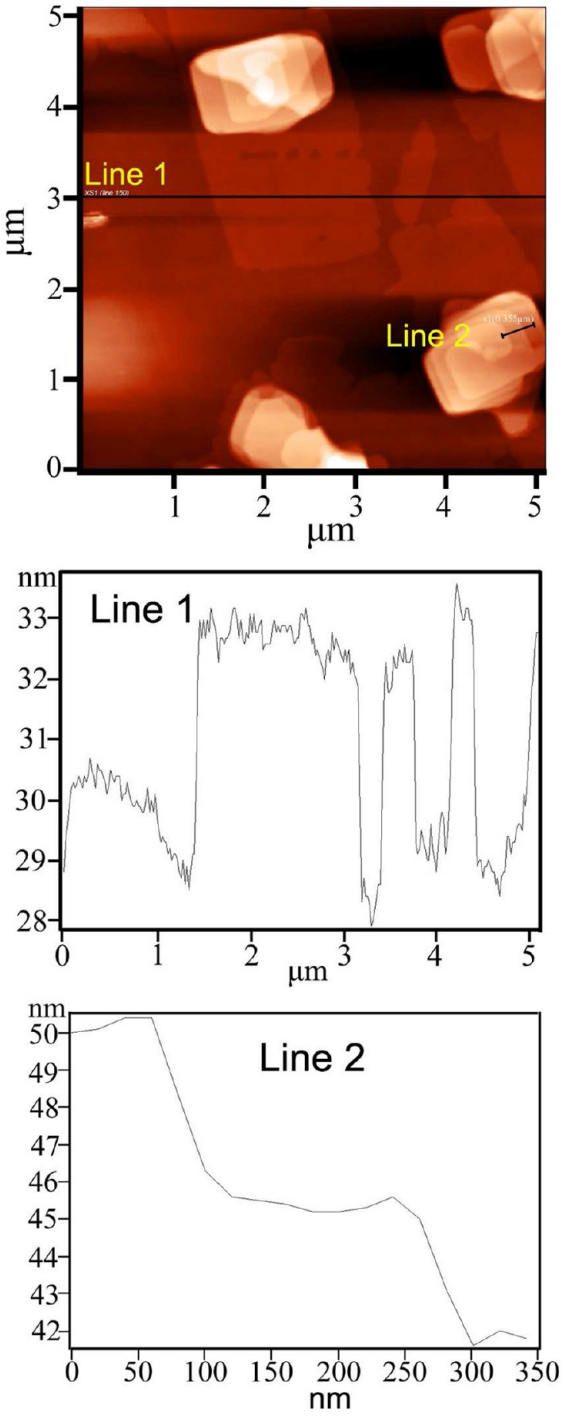

Figure 2. AFM images of the WO_3 nanosheet and the corresponding high profiles for Line 1 and Line 2.

dimensions, and their crystalline orientations are visible (Figure 7). The oriented attachment mechanism is an important and particular aggregation process happening in the solution system.[22] Upon crystal growth, the directional alignment of primary nanoparticles tries to minimize the most energetically unfavorable surface facets by fast growth perpendicular to the respective facet.[23,24] Similar assembly of PbS crystal seeds to form ultrathin 2D nanosheets has been observed.[3] In the present case, the primary tiny WO_3 nanocrystals with SLPAD route starts the anisotropic growth and tends to directionally self-aggregate or self-organize slowly parallel to the ⟨100⟩ and

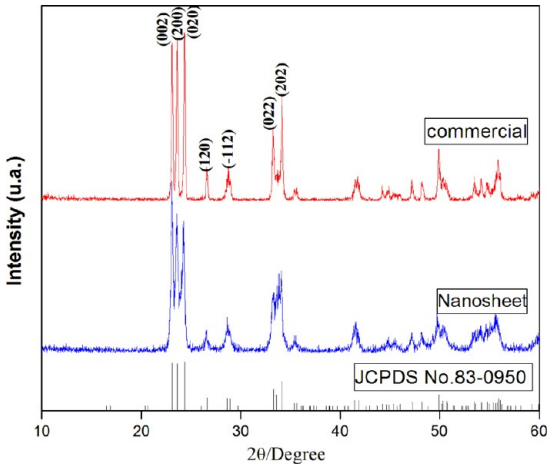

Figure 3. XRD patterns of the commercial WO_3 powder and nanosheet.

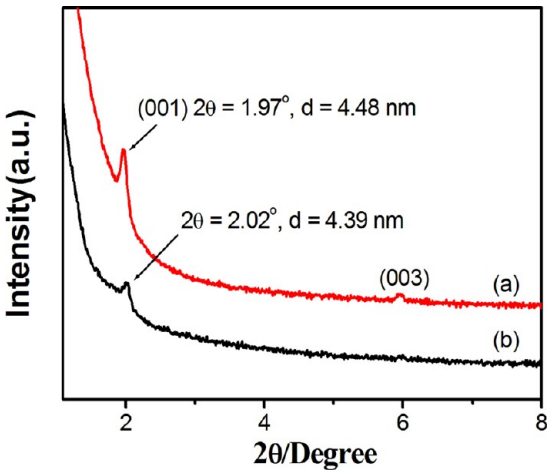

Figure 4. Small angle X-ray patterns of (a) the WO_3 nanosheet and (b) the WO_3 nanoparticle formed at the early stage.

⟨010⟩ axes to form nanosheets through an oriented attachment process by probably consuming {110} facets. The thickness remains constant during the platelet formation. The formation

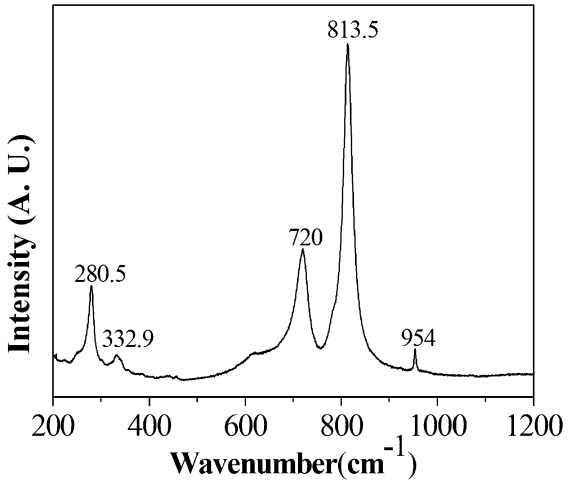

Figure 5. Raman spectrum of the WO_3 nanosheet.

dx.doi.org/10.1021/am300661s | ACS Appl. Mater. Interfaces 2012, 4, 3372−3377

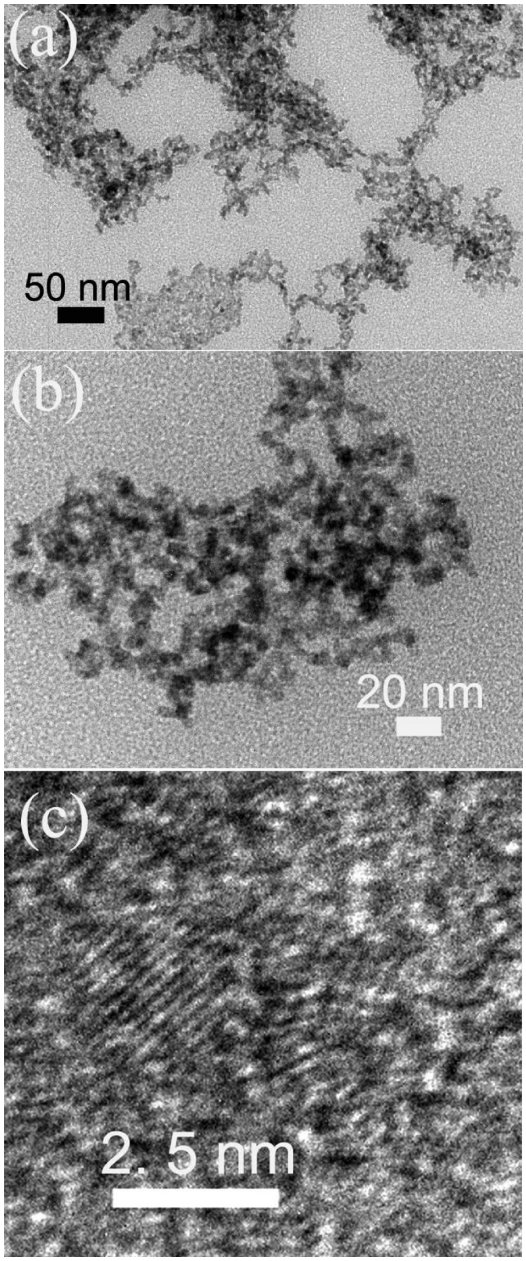

Figure 6. (a and b) TEM and (c) HRTEM images of the WO_3 nanoparticles formed at the early stage.

process of the nanosheet derived from the nanocrystals was schematically illustrated in Figure 8.

As a photocatalytic material, stoichiometric WO_3 has a conduction band (CB) edge, which is positioned slightly more positive [versus NHE (normal hydrogen electrode)] than the H_2/H_2O reduction potential and a valence band (VB) edge much more positive than the H_2O/O_2 oxidation potential,[25] which makes WO_3 capable of efficiently splitting water into oxygen and photo-oxidizing a wide range of organic compounds.[26] Reduction of CO_2 to valuable hydrocarbons using solar energy is one of the best solutions to both the global warming and the energy shortage problems.[27,28] Nevertheless, the WO_3 microcrystal proves incapable of photocatalytic reduction of CO_2 in the presence of water due to more positive CB level than the CO_2 redox potential.[29] Nanostructuring of WO_3 can greatly enhance its photocatalytic

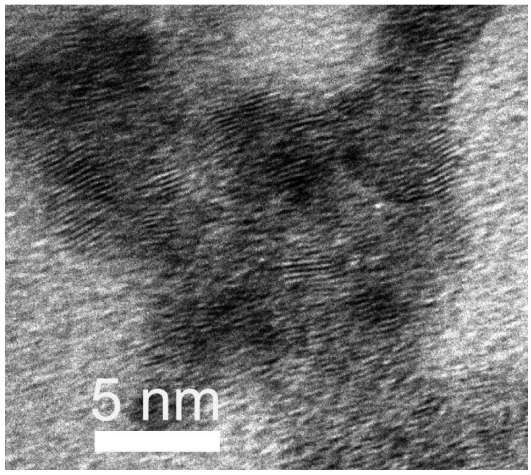

Figure 7. HRTEM images of the nanoparticles fusing together by 2D orientation attachment.

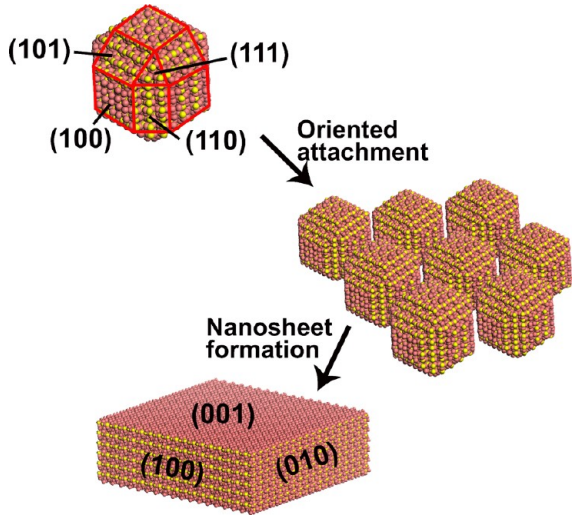

Figure 8. Schematic illustration of the WO_3 nanosheet formation from small nanocrystals.

capability. The UV−vis absorption spectra show the great blue shift of the absorption onset of the nanosheet relative to commercial WO_3 microcrystals, exhibiting quantum size effect (Figure S3, Supporting Information). The derived band gap of the nanosheet was approximately 2.79 eV, larger than that of commercial powder (2.63 eV).[30] In accordance with the reported dimensions, no quantum confinement is expected in the lateral direction, whereas the structures should be strongly confined vertically due to their extremely small thickness. The edge of the VB of WO_3 nanosheets was determined from the electron emission spectrum by means of a linear extrapolation of the onset of the VB emission[31] to be 2.37 eV (Figure S4a, Supporting Information), more positive than $E^\circ_{(H2O/H^+)}$ ($H_2O \rightarrow {}^1/_2O_2 + 2H^+ + 2e^-$, $E^\circ_{ox} = 0.82$ V vs NHE) (Figure 9). The edge of the CB was thus estimated to be −0.42 V, which is more negative than $E^\circ_{(CO2/CH4)}$ ($CO_2 + 8e^- + 8H^+ \rightarrow CH_4 + 2H_2O$, $E^\circ_{red} = -0.24$ V vs NHE). This indicates that the photogenerated electrons and holes in the irradiated WO_3 nanosheets can react with adsorbed CO_2 and H_2O to produce CH_4, as described in the following equation: $CO_2 + H_2O \rightarrow CH_4 + O_2$. In contrast, the calculated CB of the commercial powder is about 0.05 eV, more positive than $E^\circ_{red\ (CO2/CH4)}$,

dx.doi.org/10.1021/am300661s | ACS Appl. Mater. Interfaces 2012, 4, 3372−3377

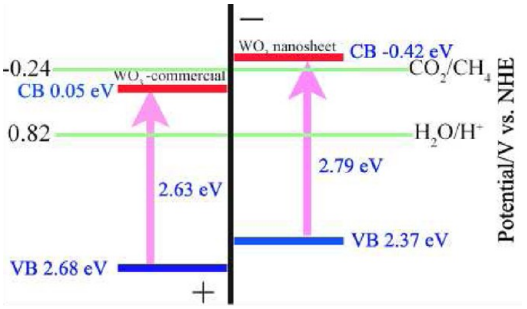

Figure 9. Calculated band positions of the WO_3 nanosheet and commercial WO_3, relative to the redox potential of CO_2/CH_4 in the presence of water.

which is unable to reduce CO_2. Figure 10 shows that the WO_3 nanosheet renders an increase of the amount of CH_4 under

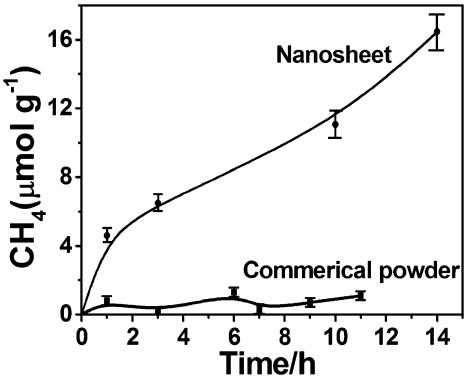

Figure 10. CH_4 generation over the nanosheet and commercial powder as a function of visible light irradiation times (λ > 420 nm).

continuous visible light illumination. The photocatalytic reaction system was filled with N_2 instead of CO_2 as comparison. With the same photocatalytic condition, no hydrocarbon species were detected. It supports that the CH_4 in the present work originates from incoming CO_2 rather than impurities or adsorbates.[32,33] A CO_2 reduction experiment performed in the dark or in the absence of the photocatalysts showed no appearance of CH_4, proving that the CO_2 reduction reaction is driven by light with the photocatalysts. In contrast, commercial WO_3 powder exhibits neglectable efficiency toward photoreduction of CO_2. Ultrathin geometry of the nanosheet is also favorable for charge carriers for fast mobility from the interior onto the surface to participate in the photoreduction reaction.

CONCLUSIONS

An ultrathin, single-crystal WO_3 nanosheet of ~4−5 nm in thickness, close to the Bohr radius for the material and corresponding to six repeating unit cell of monoclinic WO_3 along *c* axis, was synthesized with laterally oriented attachment of tiny WO_3 nanocrystals formed using a solid−liquid phase arc discharge route in an aqueous solution. Size-quantization effects in this ultrathin nanostructure allow altering the WO_3 band gap to enable the nanosheet to exhibit enhanced performance for photocatalystic reduction of CO_2 in the presence of water in hydrocarbon fuels that do not exist in its bulk form.

ASSOCIATED CONTENT

Supporting Information

TEM images and UV−vis absorption and XPS spectra. This material is available free of charge via the Internet at http://pubs.acs.org.

AUTHOR INFORMATION

Corresponding Author

*E-mail: zhouyong1999@nju.edu.cn; zgzou@nju.edu.cn.

Notes

The authors declare no competing financial interest.

ACKNOWLEDGMENTS

This work was supported by 973 Programs (No. 2011CB933300/2011CB933303), JST-MOST (No. 2009DFA61090), JSPS-NSFC (No. 20811140087), NSFC (No. 20971048 and 50732004), Fundamental Research Funds for the Central Universities (No. 1113020401 and 1115020405), and Open Research Fund of State Key Laboratory of Bioelectronics Southeast University.

REFERENCES

(1) Ma, R. Z.; Sasaki, T. *Adv. Mater.* **2010**, *22*, 5082.
(2) (a) Tang, Z. Y.; Zhang, Z.; Wang, Y.; Glotzer, S. C.; Kotov, N. A. *Science* **2006**, *314*, 274. (b) Ithurria, S.; Bousquet, G.; Dubertret, B. *J. Am. Chem. Soc.* **2011**, *133*, 3070.
(3) Schliehe, C.; Juarez, B. H.; Pelletier, M.; Jander, S.; Greshnykh, D.; Nagel, M.; Meyer, A.; Foerster, S.; Kornowski, A.; Klinke, C.; Weller, H. *Science* **2010**, *329*, 550−553.
(4) Yu, T.; Lim, B.; Xia, Y. *Angew. Chem., Int. Ed.* **2010**, *49*, 4484.
(5) (a) Vemuri, R. S.; Bharathi, K. K.; Gullapalli, S. K.; Ramana, C. V. *ACS Appl. Mater. Interfaces* **2010**, *2*, 2623. (b) Vemuri, R. S.; Engelhard, M. H.; Ramana, C. V. *ACS Appl. Mater. Interfaces* **2012**, *4*, 1371.
(6) Hong, K. Q.; Yin, W. C.; Wu, H. S.; Gao, J.; Xie, M. H. *Nanotechnology* **2005**, *16*, 1608.
(7) Yaacob, M. H.; Breedon, M.; Kalantar-zadeh, K.; Wlodarski, W. *Sens. Actuators, B* **2009**, *137*, 115.
(8) Ou, J. Z.; Yaacob, M. H.; Breedon, M.; Zheng, H. D.; Campbell, J. L.; Latham, K.; Plessis, J. D.; Wlodarski, W.; Kalantar-zadeh, K. *Phys. Chem. Chem. Phys.* **2011**, *13*, 7330.
(9) See review: Zheng, H. D.; Ou, J. Z.; Strano, M. S.; Kaner, R. B.; Mitchell, A.; Kalantar-zadeh, K. *Adv. Funct. Mater.* **2011**, *21*, 2175.
(10) Sadek, A. Z.; Zheng, H. D.; Breedon, M.; Bansal, V.; Bhargava, S. K.; Latham, K.; Zhu, J. M.; Yu, L. S.; Hu, Z.; Spizzirri, P. G.; Wlodarski, W.; Kalantar-zadeh, K. *Langmuir* **2009**, *25*, 9545.
(11) Jiao, Z. H.; Wang, J. M.; Ke, L.; Sun, X. W.; V. Demir, H. *ACS Appl. Mater. Interfaces* **2011**, *3*, 229.
(12) Amano, F.; Li, D.; Ohtani, B. *Chem. Commun.* **2010**, *46*, 2769.
(13) Su, J. Z.; Feng, X. J.; Sloppy, J. D.; Guo, L. J.; Grimes, C. A. *Nano Lett.* **2011**, *11*, 203.
(14) Widenkvist, E.; Quinlan, R. A.; Holloway, B. C.; Grennberg, H.; Jansson, U. *Cryst. Growth Des.* **2008**, *8*, 3750.
(15) Kalantar-zadeh, K.; Vijayaraghavan, A.; Ham, M.-H.; Zheng, H.; Breedon, M.; Strano, M. S. *Chem. Mater.* **2010**, *22*, 5660.
(16) Kalantar-zadeh, K.; Tang, J.; Wang, M.; Wang, K. L.; Shailos, A.; Galatsis, K.; Kojima, R.; Strong, V.; Lech, A.; Wlodarski, W.; Kaner, R. B. *Nanoscale* **2010**, *2*, 429.
(17) Chen, D. L.; Gao, L.; Yasumori, A.; Kuroda, K.; Sugahara, Y. *Small* **2008**, *4*, 1813.
(18) Wolcott, A. W.; Kuykendall, T. R.; Chen, W.; Chen, S. W.; Zhang, J. Z. *J. Phys. Chem. B* **2006**, *110*, 25288.
(19) May, R. A.; Kondrachova, L.; Hahn, B. P.; Stevenson, K. J. *J. Phys. Chem. C* **2007**, *111*, 18251.

(20) (a) Zhou, Y.; Yu, S. H.; Cui, X. P.; Wang, C. Y.; Chen, Z. Y. *Chem. Mater.* **1999**, *11*, 545. (b) Yu, S. H.; Yao, W. T.; Zhou, Y.; Jiang, J.; Wu, Q. S.; Zhang, L.; Jiang, J. *J Phys. Chem. B* **2005**, *109*, 14011.
(21) Hu, R.; Wu, H. S.; Hong, K. Q. *J. Mater. Res.* **2009**, *24*, 187.
(22) Penn, R. L.; Banfield, J. F. *Science* **1998**, *281*, 969.
(23) Pacholski, C.; Kornowski, A.; Weller, H. *Angew. Chem., Int. Ed.* **2002**, *41*, 1188.
(24) Jun, Y. W.; Casula, M. F.; Sim, J. H.; Kim, S. Y.; Cheon, J.; Alivisatos, A. P. *J. Am. Chem. Soc.* **2003**, *125*, 15981.
(25) Gratzel, M. *Nature* **2001**, *414*, 338.
(26) (a) Abe, R.; Takami, H.; Murakami, N.; Ohtani, B. *J. Am. Chem. Soc.* **2008**, *130*, 7780. (b) Chen, D.; Ye, J. H. *Adv. Funct. Mater.* **2008**, *18*, 1922.
(27) Roy, S. C.; Varghese, O. K.; Paulose, M; Grimes, C. A. *ACS Nano* **2010**, *4*, 1259.
(28) Zhou, Y.; Tian, Z.; Zhao, Z.; Liu, Q.; Kou, J.; Chen, X.; Gao, J.; Yan, S.; Zou, Z. *ACS Appl. Mater. Interfaces* **2011**, *3*, 3594.
(29) Inoue, T.; Fujishima, A.; Konishi, S.; Honda, K. *Nature* **1979**, *277*, 637.
(30) Gillet, M.; Aguir, K.; Lemire, C.; Gillet, E.; Schierbaum, K. *Thin Solid Films* **2004**, *467*, 239.
(31) Nikolay, T.; Larina, L.; Shevaleevskiy, O.; Ahn, B. T. *Energy Environ. Sci.* **2011**, *4*, 1480.
(32) Yang, C. C.; Yu, Y. H.; van der Linden, B.; Wu, J. C. S.; Mul, G. *J. Am. Chem. Soc.* **2010**, *132*, 8398.
(33) Yui, T.; Kan, A.; Saitoh, C.; Koike, K.; Ibusuki, T.; Ishitani, O. *ACS Appl. Mater. Interfaces* **2011**, *3*, 2594.